Acta Materialia 145 (2018) 196–209

Contents lists available at ScienceDirect

Acta Materialia

journal homepage: www.elsevier.com/locate/actamat

Full length article

Effect of ferrite-to-austenite phase transformation path on the interface crystallographic character distributions in a duplex stainless steel

N. Haghdadi [a], P. Cizek [a], P.D. Hodgson [a], V. Tari [b], G.S. Rohrer [b], H. Beladi [a, *]

[a] Institute for Frontier Materials, Deakin University, Waurn Ponds, VIC 3216, Australia
[b] Department of Materials Science and Engineering, Carnegie Mellon University, Pittsburgh, PA 15213-3890, USA

ARTICLE INFO

Article history:
Received 14 August 2017
Received in revised form
27 November 2017
Accepted 29 November 2017
Available online 18 December 2017

Keywords:
Interface plane distribution
Habit plane
Phase transformation path
Crystallography
Orientation relationship
Duplex stainless steel

ABSTRACT

The effect of the ferrite to austenite phase transformation route on the microstructure and interface plane character distributions was studied in a duplex stainless steel. Two markedly different austenite morphologies (i.e., equiaxed and Widmanstätten) were produced through diffusional (slow cooling) and semi-shear (air-cooling) transformations, respectively. Both austenite morphologies had textures similar to the as-received condition, which was attributed to a "texture memory" effect. The air-cooled microstructure displayed a significantly higher content of Kurdjumov-Sachs (K-S) and Nishiyama-Wassermann (N-W) interfaces (39%) compared with the slow-cooled one (16%), due to the change in the austenite nucleation and growth mechanism during the phase transformation. A five-parameter analysis of different interfaces revealed that for K-S/N-W orientation relationships, ferrite and austenite terminated on (110) and (111) planes, respectively, regardless of the transformation route. The population of these planes, however, increased as the transformation rate increased. A higher fraction of Σ3 boundaries was observed in the equiaxed austenite morphology compared with its Widmanstätten counterpart, which was mainly attributed to the different kinetics and the growth mode of austenite plates during the phase transformation. Σ9 boundaries were mostly formed where two Σ3 boundaries met and were largely of tilt character because of geometric constraints. The intervariant boundary plane distributions of both austenite microstructures displayed more frequent {111} orientations than other planes for a majority of the boundaries. This trend was markedly stronger for Widmanstätten austenite.

1. Introduction

One current goal of metals research is to develop alloys with microstructures optimized for the property of interest through cost-effective processing route/s. The types of grain boundaries and internal interphases within a polycrystalline material are known to influence its bulk properties [1–3]. Thermomechanical processing (e.g., recrystallization) is the most common route to manipulate the character of grain boundaries and interphases in materials [1–4]. It should be emphasised, though, that most technologically important metallic materials (e.g., steels and Ti alloys) do not preserve their high-temperature microstructure (i.e., recrystallized microstructure) and undergo a phase transformation on cooling [5]. In this context, a detailed knowledge on how the transformation route affects the boundary/interphase population and character would shed more light on the field of microstructural engineering.

Steels, the most industrially used metals, undergo two different phase transformations during cooling to ambient temperature from the high temperature liquid state, including delta-ferrite to austenite and subsequent austenite to ferrite (or bainite/martensite depending on the cooling rate) [6,7]. Recent studies of the latter transformation showed that the phase transformation mechanism significantly alters both population and crystallography of grain boundary planes [8–10]. This was attributed to the crystallographic constraints imposed by the phase transformation mechanism; this is distinct from the minimization of grain boundary energy that normally occurs during grain growth [8–10]. Similarly, the reverse phase transformation (i.e., ferrite to austenite) may proceed by different mechanisms depending on processing routes. However, because of the high temperatures at which austenite is stable in

* Corresponding author.
E-mail address: hossein.beladi@deakin.edu.au (H. Beladi).

https://doi.org/10.1016/j.actamat.2017.11.057
1359-6454/

plain carbon steels and the complexities associated with the microstructural observations at these temperatures, it is difficult to investigate these transformations when they actually occur [11,12].

Duplex stainless steels, developed through altering the Ni and Cr content in typical stainless steels [13], undergo the ferrite-to-austenite transformation during cooling to ambient temperature. This makes them ideal model alloys to study the ferrite-to-austenite phase transformation and, in particular, to elucidate how the transformation path affects the microstructure and the characteristics of the interfaces formed. Furthermore, from a practical point of view, it has been reported that the austenite-ferrite and austenite-austenite interface characteristics, which are largely controlled by the phase transformation path, extensively influence the micro-deformation [14], restoration [15], superplasticity [16], and precipitation behaviour [17] of these types of steels.

To comprehensively study the interface/boundary between two adjacent crystals, five independent crystallographic parameters are needed. It is convenient to use three to define the lattice misorientation and two to describe the plane orientation [18]. Recent developments in coupling conventional (2D) EBSD data with a stereological analysis have made it possible to statistically measure all parameters of the interfaces in different polycrystalline materials [18]. This approach was successfully implemented for a wide range of single [19–22] and two-phase microstructures [23–25]. A full analysis of the interfaces formed under varied body centred cubic (bcc) to face centred cubic (fcc) transformation paths is however lacking in the literature. The aim of the current study is, therefore, to examine the effect of the phase transformation mechanisms on the characteristics of the interfaces formed through the ferrite-to-austenite transformation in a model duplex stainless steel using an automated stereographic analysis approach. The main motivation is to gain an insight into how the transformation mechanism controls the characteristics of austenite-austenite and austenite-ferrite interfaces. Considering the previously reported effects of austenite/austenite and austenite/ferrite character on precipitation [17], hot working restoration processes [15] and deformation mechanisms [14] in these steels, this study would ultimately enable the design of an optimum microstructure for the property of interest.

2. Experimental

A (2205) duplex stainless steel with the chemical composition of 0.036 C, 0.321 Si, 1.82 Mn, 0.013 P, 23.2 Cr, 5.6 Ni, 2.90 Mo, 0.034 Co, 0.153 Cu, 0.245 N and balance Fe (in wt. %) was used in the current study. The steel was initially received as a 20 mm thick hot-rolled plate from which two samples having the size of ~$10 \times 10 \times 20$ mm^3 were cut. The samples were reheated to 1370 °C in a muffle furnace, in an argon-protected atmosphere, and isothermally held for 40 min to obtain a fully delta ferritic microstructure through the austenite-to-ferrite reverse transformation. They were subsequently subjected to different cooling schedules. One specimen was slowly furnace-cooled from 1370 °C to 970 °C within 48 h (with a mean cooling rate of ~0.002 °C/s) and then water-quenched to avoid the precipitation of deleterious phases (e.g., sigma, Chi and CrN), which have been reported to form at temperatures below 950 °C [26]. This heat treatment resulted in a two-phase microstructure consisting of an equiaxed austenite distributed in the matrix of delta ferrite. The latter is called ferrite hereafter. The other specimen was air-cooled from 1370 °C to room temperature. Such an increase in the cooling rate led to the formation of Widmanstätten-like austenite from the parent ferrite. Both of the heat treatment routes resulted in a similar volume fraction of austenite (48 ± 5%). The two-phase microstructures containing equiaxed and Widmanstätten austenite were subjected to a detailed microstructural study and will be referred to as "microstructure E" and "microstructure W", respectively, throughout the text.

Energy dispersive X-ray spectroscopy (EDS) was used to measure the austenite and ferrite chemical compositions for different microstructures in a JEOL JSM 7800 F FEG-SEM, equipped with an Oxford X-max 50 mm^2 EDS detector, operated at 20 kV. A transmission electron microscopy (TEM) examination of thin foils was carried out employing a JEOL JEM 2100 F microscope operated at 200 kV. Convergent-beam Kikuchi patterns were used to obtain local crystallographic orientations and misorientations. Crystallographic textures of the as-received, E, and W microstructures were measured by means of a PANalytical X'Pert X-ray diffractometer. This was carried out using Cu Kα radiation in a point focus mode. Rolling direction-normal direction (RD/ND) sections, in relation to the original hot-rolled plate, were mirror-polished and subjected to the texture measurement. As the parent ferrite grains were quite coarse, a stage oscillation technique with 10 mm of linear movement was employed to cover a large area (~14×12 mm^2) of the surface. The orientation distribution function (ODF) of the austenite and ferrite was calculated in the LaboTex3.0 texture analysis software, using four different austenite pole figures ({111}, {200}, {220} and {311}) and three different ferrite pole figures ({110}, {211} and {222}).

To characterize the interfaces/grain boundaries in different conditions, electron backscatter diffraction (EBSD) measurements were performed on the RD/ND section of the samples. The samples were mechanically polished with the last stage being a 0.3 μm oxide polishing suspension (OPS). For the different microstructures, several EBSD scans were acquired using an FEI Quanta 3-D FEG SEM. The beam voltage and current were 20 kV and 8 nA, respectively, and the working distance was ~12 mm. Totally, an area of ~60 mm^2 was scanned for the E and W microstructures to ensure statistically representative data for the further interface plane character distribution analysis. The step size was 1 μm and the grid was hexagonal. The average confidence index was at least 0.70 for all the EBSD maps. Once the maps were collected, they were subjected to several cleaning routines. At first, an iterative grain dilation routine with a 5 pixels grain size minimum was applied to remove spurious pixels. Subsequently, a single average orientation was assigned to each individual grain using a tolerance angle of 5°. Finally, each curved grain boundary connecting two triple points was approximated by linear segments with a maximum boundary deviation of 2 pixels (i.e., 2 μm) using the approach proposed by Wright and Larsen [27]. As the microstructures consisted of two different phases, the reconstructed boundaries/interfaces were classified into three categories: ferrite/ferrite, ferrite/austenite and austenite/austenite interfaces. Further analysis was carried out on each of these interfaces to determine the interface plane character distribution using a modified automated stereological procedure discussed in detail elsewhere [18]. The austenite/ferrite interfaces were treated differently due to the presence of two distinct phases on either side of the interface. Here, the interphase plane character distribution for each phase was separately calculated, representing the austenite and ferrite habit planes [24]. The analysis was carried out with the grain boundary parameter space discretized so that there were 9 bins per 90°, which offers about 10° resolution. In the current study, 97% of the bins contained at least ten observations.

3. Results

3.1. Microstructure and texture evolution

The material in the as-received condition exhibited an ~50-50 austenite/ferrite microstructure, in which both phases were elongated along the rolling direction (Fig. 1a). Ferrite displayed a sharp {001}<110> rotated cube texture with a maximum of ~11.5 times random intensity (Fig. 1b). The austenite texture was comprised of {001}<100> Cube, {011}<211> Brass, {112}<111> Copper and {011}<100> Goss components, with a maximum intensity of ~3.3 times random (Fig. 1c). These texture components have typically been reported for single-phase austenitic and ferritic steels during hot rolling [28]. The Goss component in austenite could also be related to the hot deformation, which ends in extra shear strain, particularly adjacent to the rolling surface [29].

Ferrite grains coarsened significantly during reheating to 1370 °C and isothermal holding at this temperature for 40 min, reaching a mean size of ~360 μm. This suggests that the austenite was mostly dissolved, as it would otherwise impede the growth of the ferrite grains. As mentioned above, slow cooling in the furnace to 970 °C, followed by water-quenching, yielded microstructure E with equiaxed austenite (Fig. 2), while air-cooling resulted in microstructure W with austenite having a Widmanstätten-like morphology (Fig. 3). No sigma and/or any other intermetallic phases were formed in either microstructure.

Equiaxed austenite grains were observed mostly at the ferrite-ferrite grain boundaries growing into one grain or the other. Widmanstätten austenite grains were detected at both ferrite grain interiors and ferrite-ferrite grain boundaries. It should be noted, though, that some of the observed intragranular austenite islands might have nucleated on the grain boundaries that were not in the plane of observation (i.e., a sectioning effect) [30]. Nevertheless, the fraction of such islands is not expected to be significant, considering the large size of the ferrite grains. The austenite phase nucleated at the grain boundaries grew along the ferrite-ferrite boundaries forming a thin layer on either side of these boundaries, hereafter called allotriomorphic austenite (shown by the white arrows in Fig. 3). Small protrusions also appeared on most of the allotriomorph austenite layers, forming a finger-like austenite morphology (the black arrows in Fig. 3). There were some indications of the occasional presence of low-angle sub-boundaries at the interface of allotriomorph austenite and protruded austenite. Nevertheless, such sub-boundaries were not observed for all of the finger-like austenite islands. In this context, it should be mentioned that EBSD may not be able to resolve all low-angle sub-boundary misorientations, which can be significantly less than 1°. Because of this, further investigations were conducted in the TEM. Fig. 4 shows examples of TEM micrographs of various austenite protrusions. Fig. 4a presents an austenite-austenite low-angle boundary with a misorientation of ~1.08°. On the other hand, absence of any austenite-austenite boundary in the protrusions is illustrated in Fig. 4b. The plate-like austenite morphology, which nucleated either on the prior ferrite grain boundaries or intragranularly, was also frequently observed in microstructure W (the yellow arrows in Fig. 3).

As expected, the ferrite texture in both of the microstructures studied showed similar characteristics to the as-received condition, having a strong rotated cube {001}<110> component (Figs. 1–3). The maximum intensity was ~17.9 and ~15.6 times random for microstructures E and W, respectively. This is similar to the texture of ferrite in the as-received condition, though it was significantly strengthened. Such a texture sharpening may be attributed to the recovery and growth of ferrite grains taking place at 1370 °C [31]. Despite distinct phase transformation paths, austenite with both Widmanstätten and equiaxed morphologies displayed a very similar texture to that of the as-received material, composed of Cube, Brass, Copper and Goss components (Figs. 1–3). The maximum intensity was 4.0 and 4.2 times random for microstructures E and W, respectively. This can be mostly attributed to a "texture memory effect", implying that the final austenite texture associated with a preferential orientation relationship through a phase transformation was inherited from the texture of the initial austenite in the as-received condition. In a treatment that involves heating from austenite into ferrite and then cooling back again there will be a large number of possible final orientations, only few of which correspond to the original austenite orientation. It would,

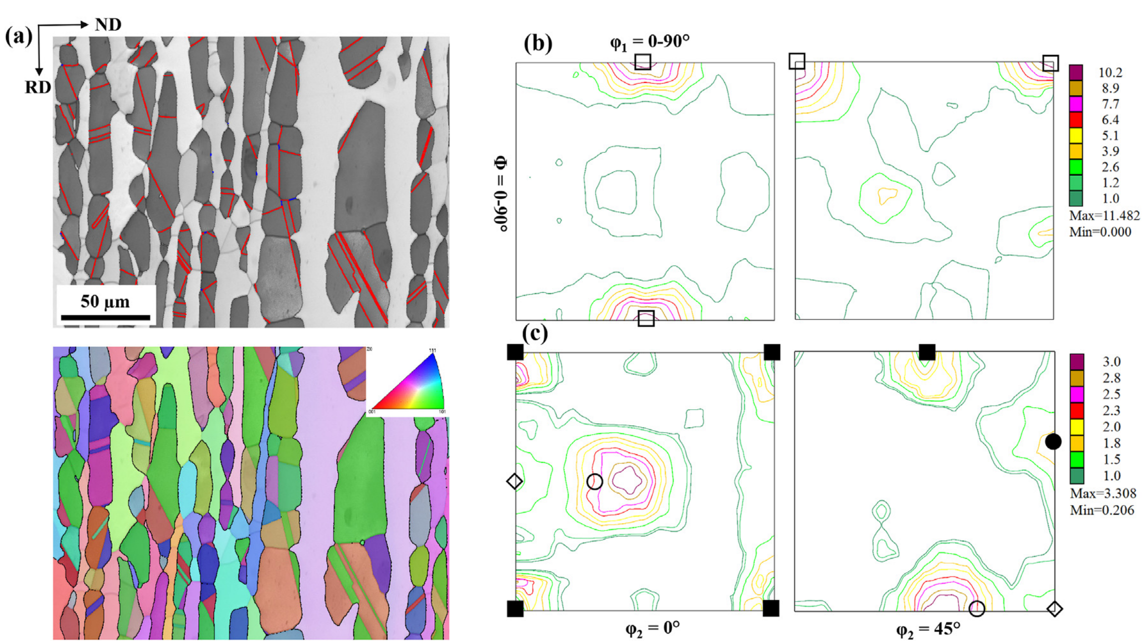

Fig. 1. (a) EBSD band contrast and IPF maps (in the transverse direction) showing the microstructure of the as-received (hot-rolled) duplex stainless steel. The dark grey and light grey areas represent austenite and ferrite, respectively. The red and blue lines are Σ3 and Σ9 CSL boundaries, respectively. Orientation distribution of (b) ferrite and (c) austenite phases in the as-received condition. □ {001} <110>; ■ {001} <100>; ○ {011} <211>; ◇ {011} <100>; ● {112}<111>. (For interpretation of the references to colour in this figure legend, the reader is referred to the Web version of this article.)

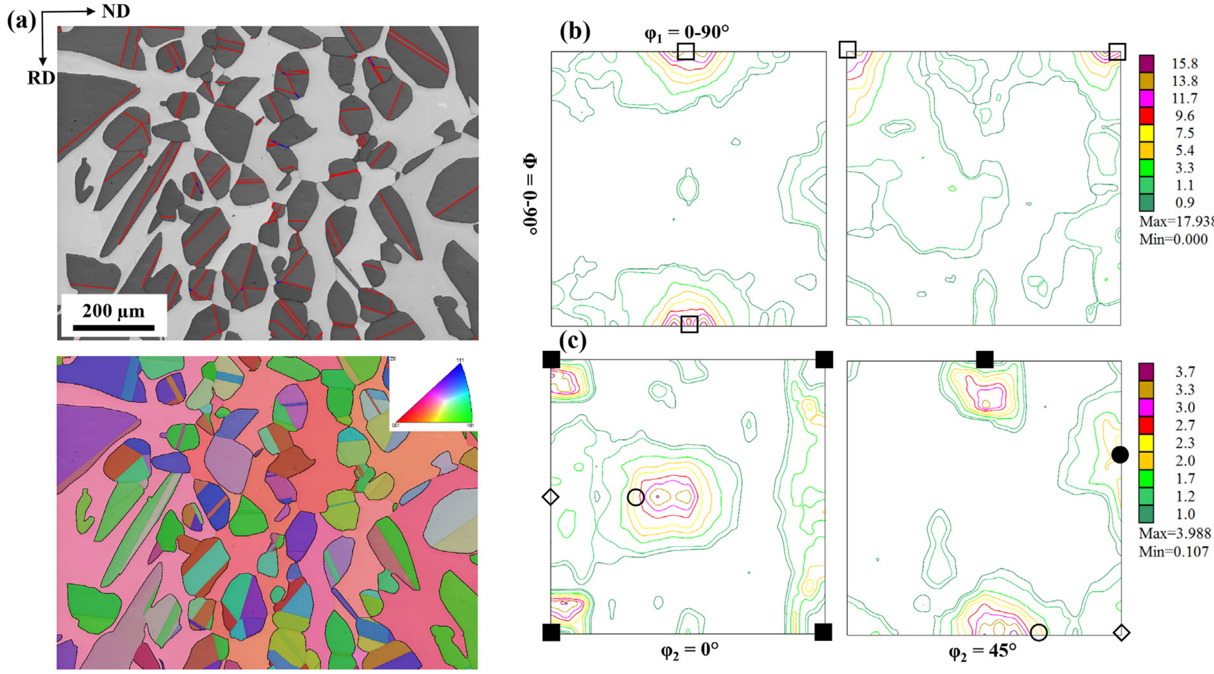

Fig. 2. (a) EBSD band contrast and IPF maps (in the transverse direction) showing the equiaxed (E) microstructure after the heat treatment at 1370 °C followed by slow cooling to 970 °C. The dark grey and light grey areas represent austenite and ferrite, respectively. The red and blue lines are Σ3 and Σ9 CSL boundaries, respectively. The orientation distribution of (b) ferrite and (c) austenite phases for the corresponding structure. □ {001} <110>; ■ {001} <100>; ○ {011} <211>; ◇ {011} <100>; ● {112}<111>. (For interpretation of the references to colour in this figure legend, the reader is referred to the Web version of this article.)

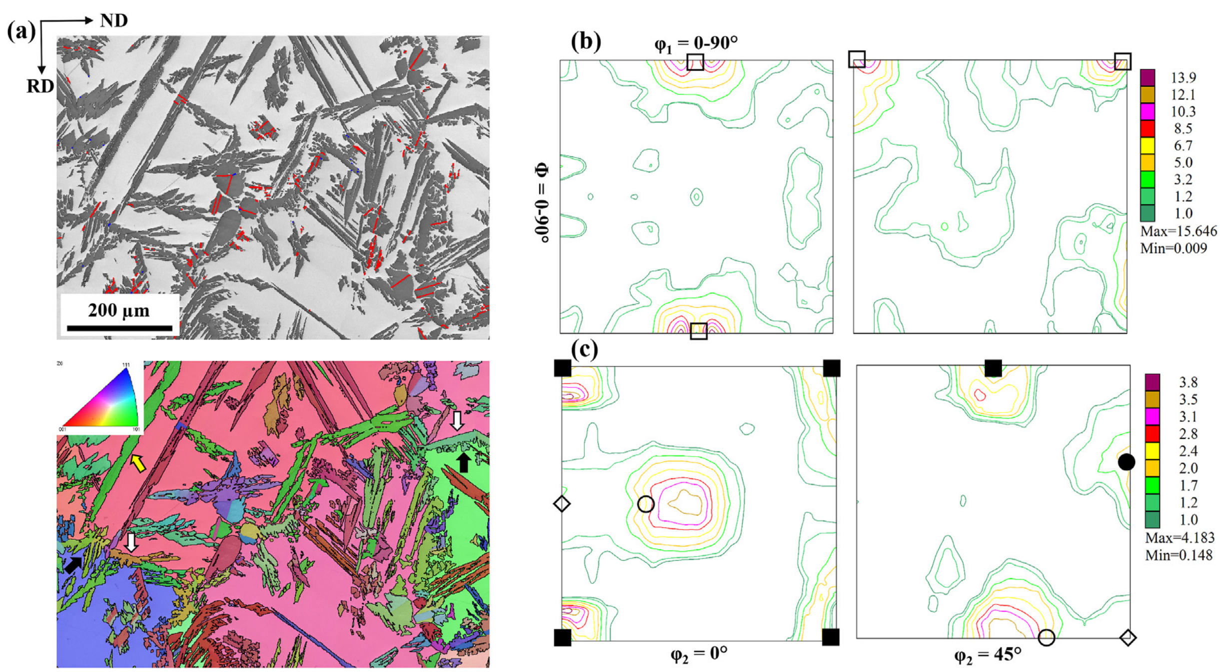

Fig. 3. (a) EBSD band contrast and IPF maps (in the transverse direction) showing the Widmanstätten (W) microstructure after the heat treatment at 1370 °C followed by air cooling to room temperature. The dark grey and light grey areas represent austenite and ferrite, respectively. The red and blue lines are Σ3 and Σ9 CSL boundaries, respectively. The orientation distribution of (b) ferrite and (c) austenite phases for the corresponding structure. □ {001} <110>; ■ {001} <100>; ○ {011} <211>; ◇ {011} <100>; ● {112}<111>. Examples of allotriomorphic austenite are shown by white arrows. Finger-like austenite protrusions are shown by black arrows. An example of an intragranular elongated austenite is shown by yellow arrows. (For interpretation of the references to colour in this figure legend, the reader is referred to the Web version of this article.)

therefore, be expected that even when the original texture is very sharp, the resulting one after the double phase transformation should be significantly weaker. In the current work, however, the final texture is stronger than would be expected, implying that there is a degree of texture memory, which is mostly attributed to variant selection [32].

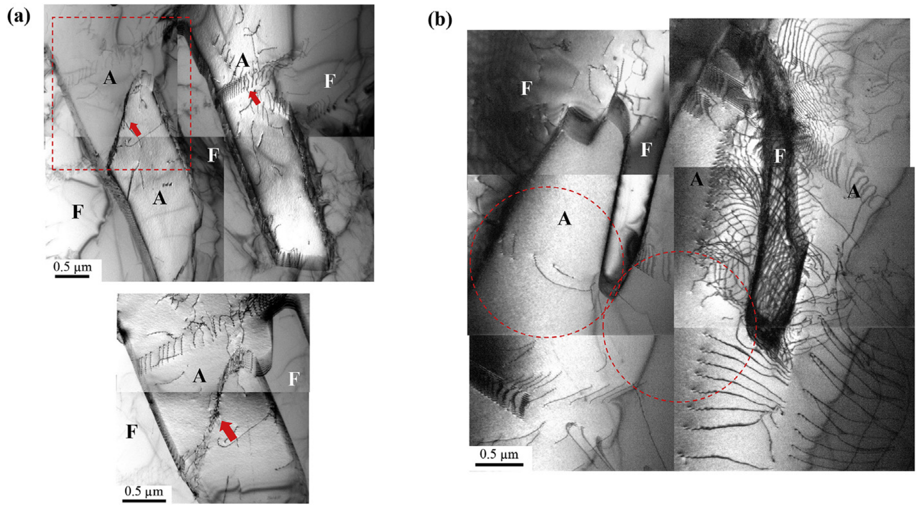

Fig. 4. (a) An example of austenite protrusions observed in microstructure W showing sub-boundaries (arrowed by red colour) indicative of the edge-on-edge sympathetic nucleation. The bottom image corresponds to the region indicated by the dashed rectangle in the top image subjected to a slight retilt, showing a low angle boundary of ~1.08°<0.045 0.736−0.675>. (b) An example of austenite protrusions observed in microstructure W lacking any austenite-austenite sub-boundary (dashed circles), indicative of the instability mechanism. F and A refer to ferrite and austenite, respectively. (For interpretation of the references to colour in this figure legend, the reader is referred to the Web version of this article.)

3.2. The characteristics of interfaces

The overall misorientation angle distribution showed distinct characteristics for microstructures E and W formed through different cooling rates from the ferrite region. For both microstructures, a broad distribution was observed in a range of 10–60°, having a sharp peak at ~60° and a relatively broad peak at around ~44° (Fig. 5a,d). The intensity of the peak at 60° was higher in microstructure E, while the peak at 44° was more pronounced in microstructure W. To study the interfaces in more detail, they were categorized into three sets, namely austenite-ferrite, austenite-austenite and ferrite-ferrite interfaces. For both microstructures, the most populated boundaries were ferrite-austenite interfaces followed by austenite-austenite and ferrite-ferrite interfaces (Table 1).

For both microstructures, the ferrite-ferrite misorientation angle distribution did not have a specific trend and was very noisy (Fig. 5b and e). Indeed, most of the initial ferrite-ferrite boundaries were consumed by the nucleation of austenite grains. Therefore, further analysis was not carried out on the ferrite-ferrite interfaces,

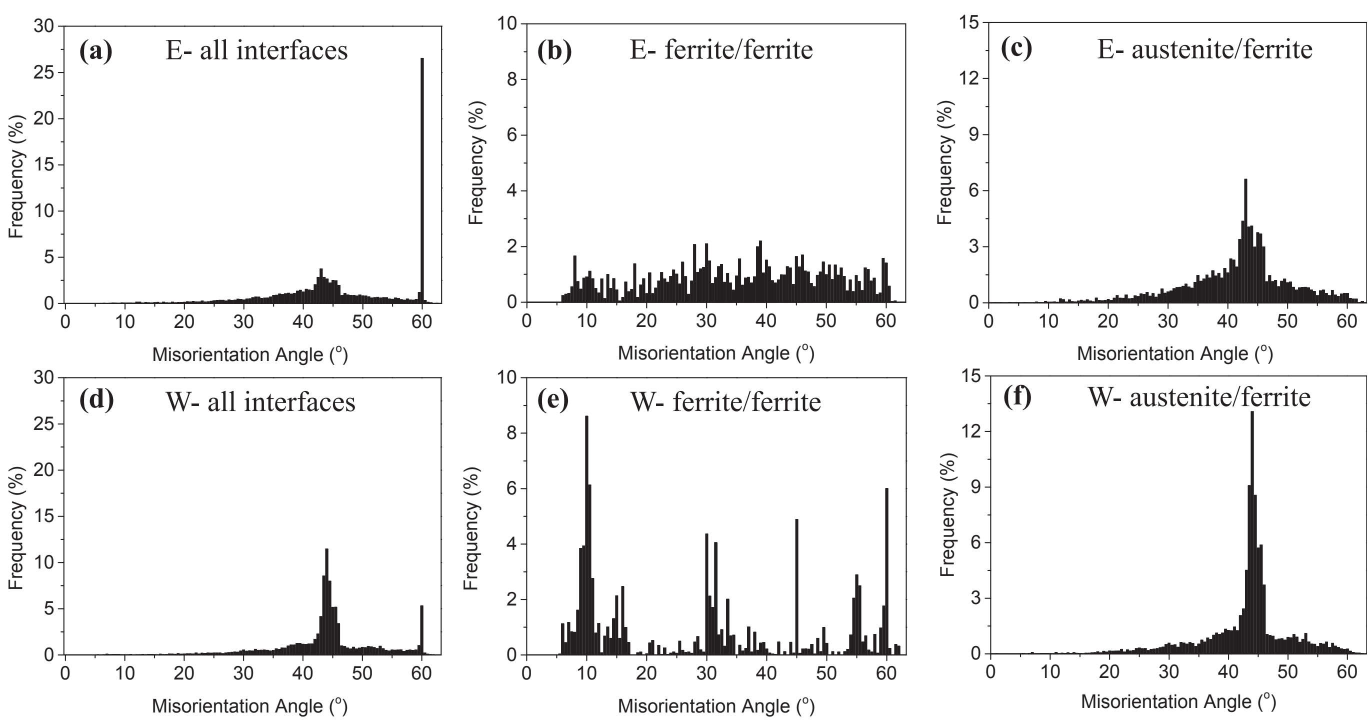

Fig. 5. Misorientation angle distribution for (a,d) all interfaces (including ferrite-ferrite, austenite-ferrite and austenite-austenite), (b,e) ferrite-ferrite, (c,f) austenite-ferrite boundaries for (a–c) microstructure E and (d–e) microstructure W.

Table 1
Number of segments for different interfaces formed in different microstructures.

Microstructure	Number of all interfaces	Ferrite/ferrite interfaces		Ferrite/austenite interfaces		Austenite/austenite interfaces	
		Number	%	Number	%	Number	%
E (Furnace cooled)	92,279	2381	2.6	66,251	71.8	23,647	25.6
W (Air cooled)	241,792	923	0.4	212,739	87.9	28,130	11.6

as only a limited number of boundaries was present.

3.2.1. Austenite-ferrite interfaces

The misorientation angle distributions for the austenite-ferrite interfaces in the E and W microstructures are shown in Fig. 5c,f. Both distributions exhibited a peak at about 42–46°, but the peak for microstructure W is about twice the intensity of the maximum for microstructure E. This misorientation angle range overlaps well with the one expected for the well-known orientation relationship models (e.g., Kurdjumov-Sachs (K-S) [33], Nishiyama-Wasserman (N-W) [34], Greninger–Troiano (G–T) [35], Pitsch (P) [36] and Bain [37]), that result from the bcc to fcc transformation (Table 2). The K-S and N-W ORs are the most versatile models developed for this phase transformation and are only 5.26° apart. For further analysis, the interfaces were classified into three groups, K-S, N-W and "others", based on misorientation. To be classified in the K-S or N-W partition, the angular deviation from the ideal misorientation had to be within 2° for that OR; all other interfaces were classified as others. It was found that there was a higher tendency towards K-S and N-W interfaces once the transformation (cooling) rate was increased. Microstructure W contained 31% and 8% of K-S and N-W boundaries, while microstructure E comprised 12% and 4% of K-S and N-W interfaces, respectively.

Using the five-parameter boundary analysis approach, the interphase boundary plane distributions were calculated for the interfaces classified as K-S, N-W and others (Fig. 6). It was found that for the K-S and N-W ORs, irrespective of the transformation path, austenite and ferrite tended to terminate on (111) and (110) orientations, respectively. In the case of the K-S OR, the intensity of (111) austenite planes and (110) ferrite planes was ~3.2 multiple random distribution (MRD) and ~2.2 MRD, respectively, for the E and W microstructures. For the N-W OR, the intensity of the interphase boundary plane distribution for both ferrite and austenite was relatively lower than for the K-S OR, though planes were similarly terminated on (110) and (111) orientations, respectively. For the other ORs, both austenite and ferrite interestingly exhibited a peak at the position of (111) plane irrespective of the phase transformation path. The peak intensity for austenite and ferrite was 2.0 MRD (2.1 MRD) and 1.5 MRD (1.6 MRD), respectively in microstructure E (W) (Fig. 6).

It is worth mentioning that the austenite in microstructure W consisted of allotriomorphic and intragranular morphologies. By separating these two morphologies using the crop command in the TSL software, it was found that the allotriomorphic austenite had a lower fraction of K-S/N-W interfaces (i.e., 23%) compared with the intragranular elongated austenite (i.e., 42%). For both of the above austenite morphologies in microstructure W, the interphase habit planes terminated in austenite and ferrite at (111) and (110) orientations, respectively, for both K-S and N-W ORs (Figs. 7 and 8). The plane distribution peaks were sharper for the intragranular austenite compared with the allotriomorph morphology. By contrast, habit plane distributions for the other interphases displayed maxima at the (111) orientation for austenite and ferrite for both austenite morphologies.

The plane character distribution for all austenite-ferrite interfaces irrespective of misorientation was also plotted in Fig. 9. The austenite had a peak at (111) position, similar to the ones observed for a specific OR, having intensities of ~2.2 MRD and ~2.4 MRD for microstructures E and W, respectively. By contrast, ferrite exhibited multiple peaks at the positions of (110) and (111) planes for both transformation paths. The most intense peak occurred at (111) with an intensity of ~1.5 MRD, followed by a peak at (110) with an intensity of ~1.4 MRD in microstructure E. On the other hand, the strongest peak for microstructure W corresponded to (110) planes with 1.6 MRD followed by a peak at (111) having an intensity of 1.4 MRD (Fig. 9).

3.2.2. Austenite-austenite interfaces

The misorientation angle distribution for the austenite-austenite boundaries showed a sharp peak at 60° for both the E and W microstructures (Fig. 10). There was also a secondary minor peak at 39°. The misorientation axes associated with these angles exhibited intensity maxima at the <111> and <110> orientations, respectively. Thus, the above peaks represent Σ3 and Σ9 boundaries, characterized by 60°/<111> and 39°/<110> angle axis pairs, respectively. Σ3 twin boundaries were frequently observed in both of the microstructures studied and their frequencies were higher in the equiaxed austenite compared with the Widmanstätten austenite microstructure. Σ9 boundaries, which mostly formed through the intersection of two Σ3 boundaries, were also evident in both austenite morphologies (Figs. 2 and 3).

The grain boundary planes of Σ3 boundaries satisfying

Table 2
Plane and direction parallelism conditions and misorientation angle–axis pairs between FCC and BCC phases under different orientation relationships.

Orientation relationship	Parallelism	Minimum angle-axis pair	Ref.
Kurdjumov-Sachs (K-S)	$\{111\}_{fcc}//\{110\}_{bcc}$ $<110>_{fcc}//<111>_{bcc}$	42.85° <0.968 0.178 0.178>	[32]
Greninger–Troiano (G–T)	$\{111\}_{fcc}//\{110\}_{bcc}$ $<123>_{fcc}//<133>_{bcc}$	44.23° <0.973 0.189 0.133>	[34]
Bain (B)	$\{100\}_{fcc}//\{100\}_{bcc}$ $<100>_{fcc}//<110>_{bcc}$	45° <1 0 0>	[36]
Pitsch (P)	$\{100\}_{fcc}//\{110\}_{bcc}$ $<110>_{fcc}//<111>_{bcc}$	45.98° <0.08 0.2 0.98>	[35]
Nishiyama-Wassermann (N-W)	$\{111\}_{fcc}//\{110\}_{bcc}$ $<112>_{fcc}//<110>_{bcc}$	45.98° <0.976 0.083 0.201>	[33]

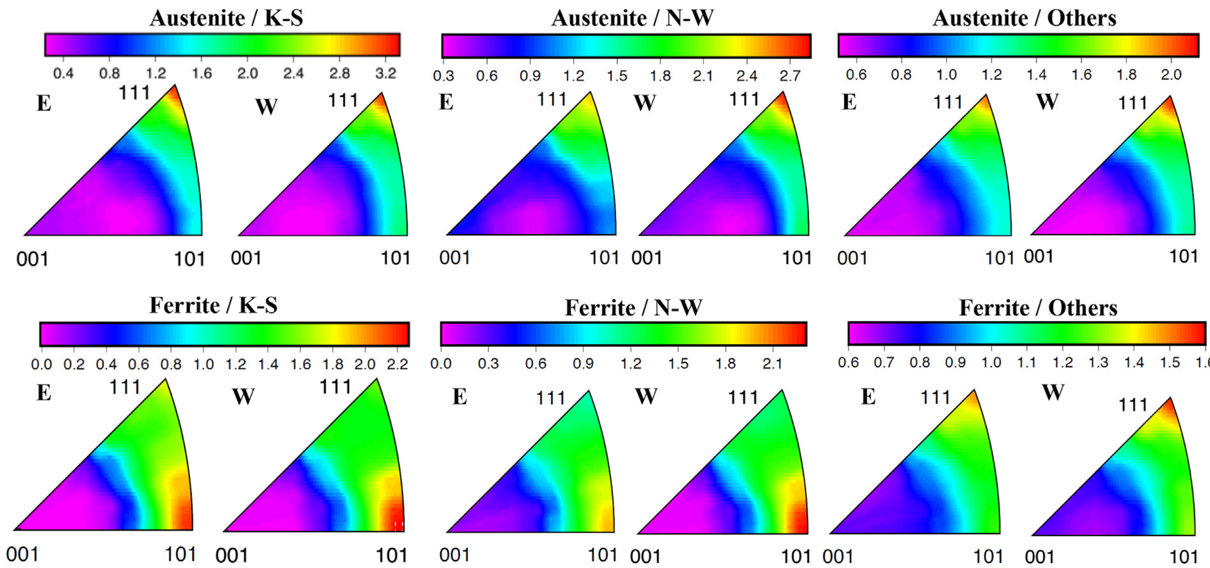

Fig. 6. Distribution of the austenite-ferrite interface boundary planes, expressed in the austenite and ferrite crystal lattice frames, for different orientation relationships of K-S, N-W and "others" in microstructure E and microstructure W. The colour scale represents multiples of a random distribution. (For interpretation of the references to colour in this figure legend, the reader is referred to the Web version of this article.)

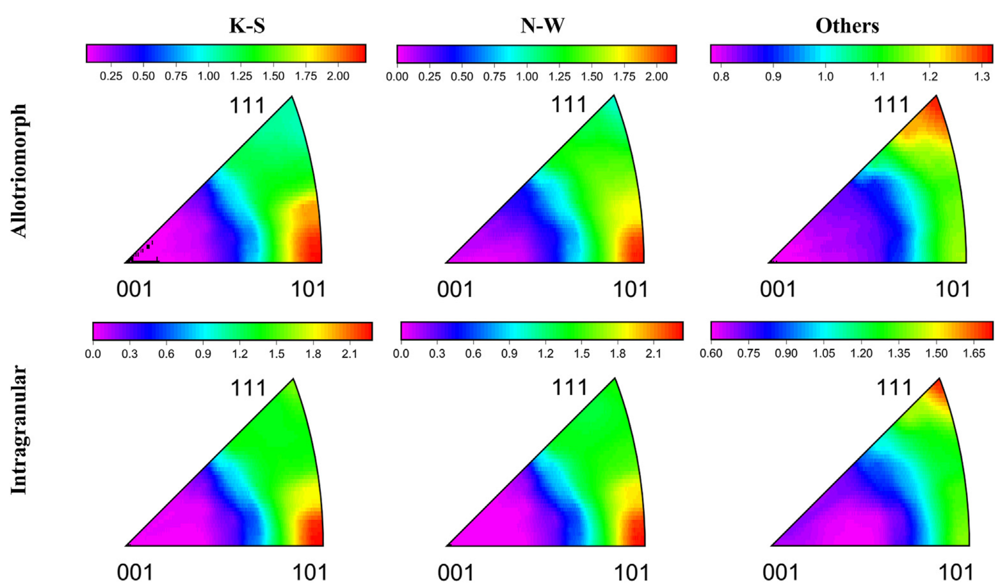

Fig. 7. Distribution of the austenite-ferrite interface boundary planes, expressed in the ferrite crystal lattice frame, for different austenite morphologies present within microstructure W for different orientation relationships. The colour scale values are in MRD. (For interpretation of the references to colour in this figure legend, the reader is referred to the Web version of this article.)

Brandon's criterion [38] were compared with the ideal twin plane orientation and the ones within $\pm 10^{\circ}$ of this orientation were considered coherent, while the rest were classified as incoherent. The extent of $\Sigma 3$ coherence was significantly influenced by the transformation path (i.e., austenite characteristics/morphology). The equiaxed austenite had a higher coherent $\Sigma 3$ fraction than the Widmanstätten austenite microstructure (Fig. 10c–d).

Fig. 11 demonstrates that the $\Sigma 3$ grain boundary character distribution for austenite exhibited a sharp peak at (111) orientation with a twist character for both phase transformation paths, though the intensity was much greater for the equiaxed austenite (i.e., 3200 MRD) compared with the Widmanstätten austenite microstructure (i.e., 2500 MRD). In this analysis, the misorientation axis was [111] so twist boundaries must have (111) orientations. Because of the bicrystal symmetry, other planes in the {111} family are not equivalent. This is a typical characteristic for $\Sigma 3$ boundaries, observed in single-phase fcc materials [19,39,40]. The distribution of $\Sigma 9$ grain boundary planes was also similar for both microstructures; the grain boundary planes were situated along the zone of tilt boundaries. This is also consistent with the previous studies of single-phase fcc materials [19,39,40].

Apart from the peaks at 39° and 60°, there were some austenite-austenite boundaries with much lower populations, which probably formed when two growing austenite grains with distinct orientations impinged on each other. For the sake of simplicity, it was assumed that the ferrite to austenite transformation follows the K-S OR. For a particular ferrite grain, 24 crystallographically equivalent K-S orientated austenite variants/orientations can be formed. The

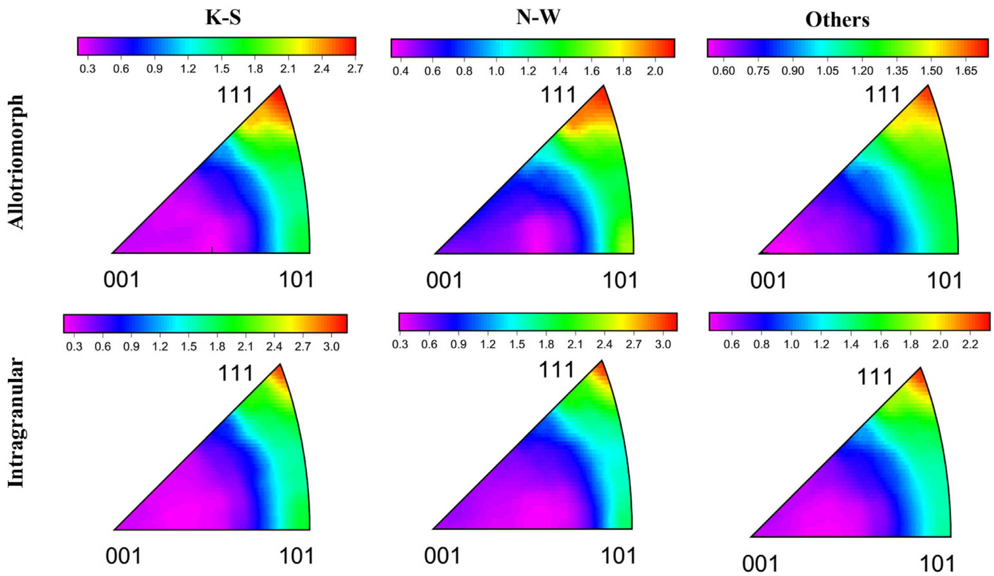

Fig. 8. Distribution of the austenite-ferrite interface boundary planes, expressed in the austenite crystal lattice frame, for different austenite morphologies present within microstructure W for different orientation relationships. The colour scale values are in MRD. (For interpretation of the references to colour in this figure legend, the reader is referred to the Web version of this article.)

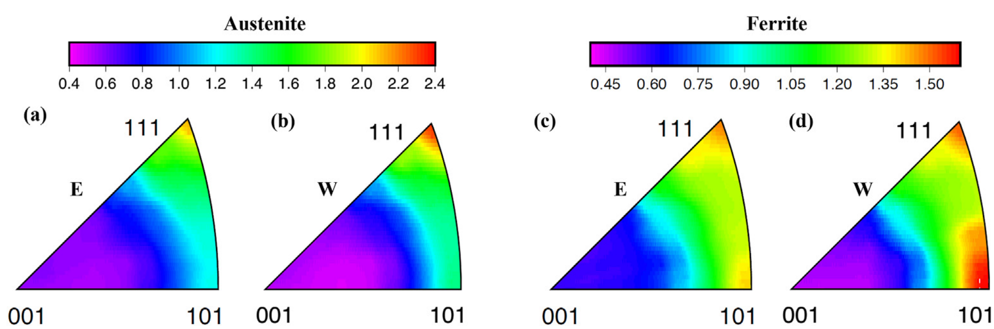

Fig. 9. Distributions of the austenite-ferrite interface boundary planes expressed in the austenite (a,b) and ferrite (c,d) crystal lattice frames for microstructures E and W, respectively. The colour scale represents multiples of a random distribution. (For interpretation of the references to colour in this figure legend, the reader is referred to the Web version of this article.)

misorientation angle/axis pairs associated with the impingement of these variants are given in Table 3. Due to the crystal symmetry, some of these intervariant interfaces are identical, therefore, 23 is reduced to only 16 distinct misorientation angle-axis pairs [9].

Fig. 12 shows the frequency of different austenite-austenite intervariants formed through different transformation paths. For comparison, the theoretical intervariant boundary frequency is also plotted, assuming that all variants are formed with equal statistical probability during the ferrite to austenite phase transformation (i.e., without variant selection). In general, the intervariant austenite/austenite boundary distributions for both the microstructures were significantly different from random variant selection. This suggests that variant selection, to some extent, took place in both the phase transformation paths. This was mostly associated with the presence of a high fraction of Σ3 boundaries (i.e., V1-V2) in both microstructures, which formed either during an early stage of austenite nuclei growth and/or through the intersection of two distinct growing austenite variants. Although V1-V4 and V1-V8 boundaries had relatively high populations in both microstructures, the frequencies of other intervariant boundaries were lower than expected if the variant selection were random. It is worth reiterating that ferrite was not fully transformed to austenite, which significantly limited the impingement of different austenite variants and this might also have contributed to the occurrence of non-random intervariant boundary fractions.

In order to compute the grain boundary plane distributions associated with the intervariants, all Σ3 and Σ9 grain boundary traces were first removed from the data set. The distribution of austenite-austenite grain boundary planes, excluding Σ3s and Σ9s, revealed a peak at the {111} orientation for both austenite morphologies (Fig. 13). However, this peak was much greater in Widmanstätten austenite than in the equiaxed austenite microstructure.

4. Discussion

The current work presents a comprehensive study on the effect of the phase transformation route on the characteristics of microstructure, texture and interfaces formed during the ferrite-to-austenite phase transformation. The results demonstrate that a change in the transformation mechanism considerably alters the microstructure and the interphase/grain boundary plane distribution, while it does not markedly influence the overall crystallographic texture. Since the austenite/austenite and austenite/ferrite interface characteristics influence different properties of this class of steels such as precipitation [17], hot working processes [15] and

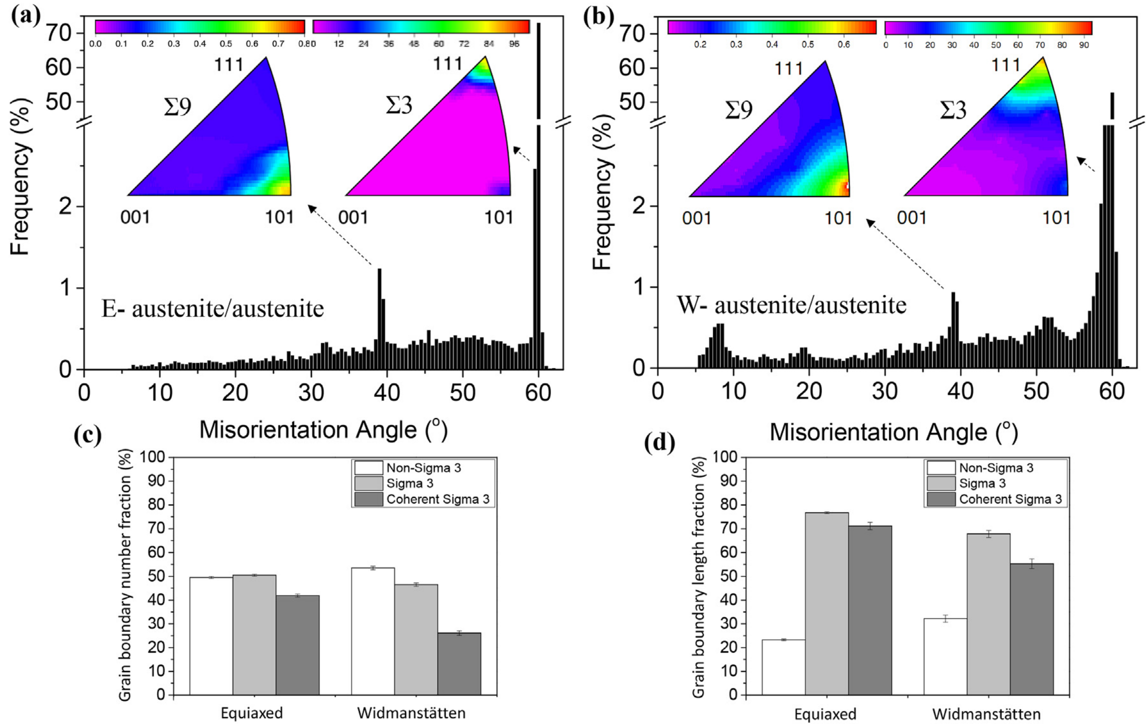

Fig. 10. Misorientation angle/axis distribution for the austenite/austenite boundaries in (a) microstructure E and (b) microstructure W. The colour scale values are in MRD. (c,d) The population and length frequency of different types of austenite/austenite boundaries in the two microstructures studied. (For interpretation of the references to colour in this figure legend, the reader is referred to the Web version of this article.)

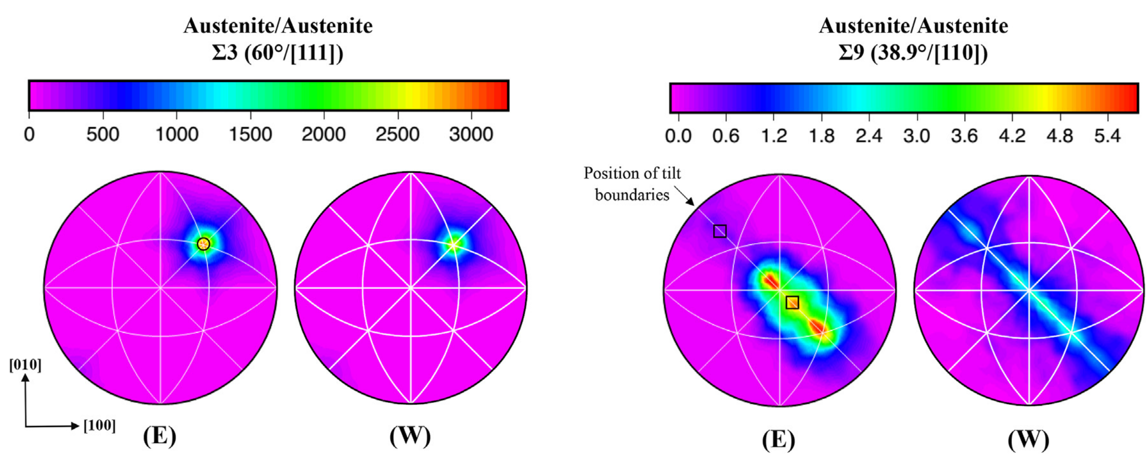

Fig. 11. Austenite-austenite grain boundary character distribution in microstructures E and W at the fixed misorientations of 60°/[111] and 38.9°/[110], plotted in the [001] stereographic projection. The squares and circles represent the positions of symmetric tilt and pure twist boundaries, respectively. The colour scale values are in MRD. (For interpretation of the references to colour in this figure legend, the reader is referred to the Web version of this article.)

deformation mechanisms [14], the current study highlights the importance of the phase transformation path on the in-service properties of duplex stainless steels.

4.1. Microstructure characteristics

The cooling rate from the ferritic region significantly affects the morphology of austenite. While an equiaxed morphology is obtained during slow cooling (Fig. 2), a Widmanstätten morphology of austenite is achieved by air-cooling (Fig. 3). The latter microstructure consists mostly of allotriomorphic and elongated intragranular austenite. During the ferrite to austenite transformation, once the lattice change occurs, elastic strain is induced. If the elastic strain is not relaxed, the phase transformation cannot proceed further. In the slow cooling condition, the phase transformation strain can be readily relaxed during diffusional transformation in the high temperatures regime. However, other mechanism/s should be involved to relax the elastic strain at a high cooling rate (e.g., air-cooling). For such transformation, a shear-assisted diffusional model has been suggested, in which the phase change is assumed to occur through atomic jumps, as in the diffusional transformation, while the elastic strain is relaxed through a lattice invariant shear by slip displacement [41,42].

The apparent intragranular austenite phase might be formed by

Table 3
Possible 24 variants generated through a phase transformation having the K–S orientation relationship [9].

Variant	Plane parallel	Direction parallel	Rotation angle/axis from V1
V1	(1 1 1)$_\gamma$ ∥ (0 1 1)$_\delta$	[−1 0 1]γ ∥ [−1 −1 1]δ	–
V2		[−1 0 1]γ ∥ [−1 1 −1]δ	60°/[1 1 −1]
V3		[0 1 −1]γ ∥ [−1 −1 1]δ	60°/[0 1 1]
V4		[0 1 −1]γ ∥ [−1 1 −1]δ	10.5°/[0−1 −1]
V5		[1 −1 0]γ ∥ [−1 −1 1]δ	60°/[0−1 −1]
V6		[1 −1 0]γ ∥ [−1 1 −1]δ	49.5°/[0 1 1]
V7	(1 −1 1)$_\gamma$ ∥ (0 1 1)$_\delta$	[1 0−1]γ ∥ [−1 −1 1]δ	49.5°/[−1 −1 1]
V8		[1 0−1]γ ∥ [−1 1 −1]δ	10.5°/[1 1 −1]
V9		[−1 −1 0]γ ∥ [−1 −1 1]δ	50.5°/[−10 3−13]
V10		[−1 −1 0]γ ∥ [−1 1 −1]δ	50.5°/[−7 −5 5]
V11		[0 1 1]γ∥ [−1 −1 1]δ	14.9°/[13 5 1]
V12		[0 1 1]γ ∥ [−1 1 −1]δ	57.2°/[−3 5 6]
V13	(−1 1 1)$_\gamma$ ∥ (0 1 1)$_\delta$	[0−1 1]γ ∥ [−1 −1 1]δ	14.9°/[5−13 −1]
V14		[0−1 1]γ ∥ [−1 1 −1]δ	50.5°/[−5 5−7]
V15		[−1 0−1]γ ∥ [−1 −1 1]δ	57.2°/[−6 −2 5]
V16		[−1 0−1]γ ∥ [−1 1 −1]δ	20.6°/[11 −11 −6]
V17		[1 1 0]γ ∥ [−1 −1 1]δ	51.7°/[−11 6−11]
V18		[1 1 0]γ ∥ [−1 1 −1]δ	47.1°/[−24 −10 21]
V19	(1 1 −1)$_\gamma$ ∥ (0 1 1)$_\delta$	[−1 1 0]γ ∥ [−1 −1 1]δ	50.5°/[−3 13 10]
V20		[−1 1 0]γ ∥ [−1 1 −1]δ	57.2°/[3 6 −5]
V21		[0−1 −1]γ ∥ [−1 −1 1]δ	20.6°/[3 0−1]
V22		[0−1 −1]γ ∥ [−1 1 −1]δ	47.1°/[−10 21 24]
V23		[1 0 1]γ ∥ [−1 −1 1]δ	57.2°/[−2 −5 −6]
V24		[1 0 1]γ ∥ [−1 1 −1]δ	21.1°/[9 −4 0]

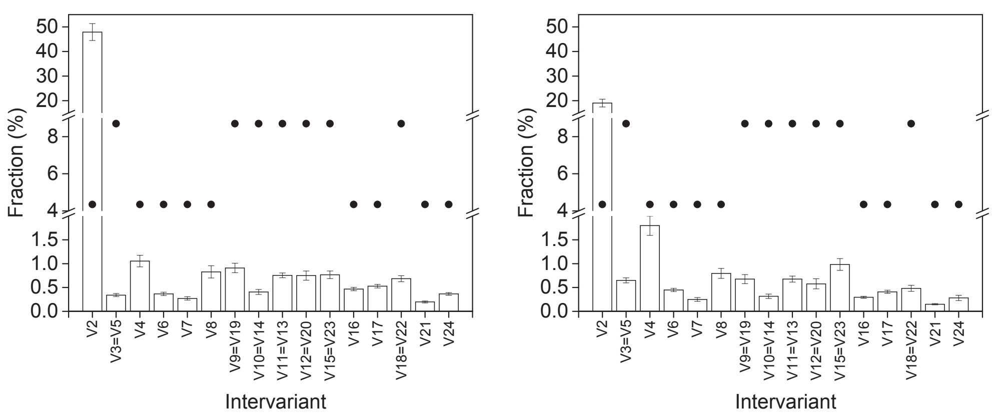

Fig. 12. Comparing inter-variant interfaces between V1 and Vi (i = 2–24) for (a) microstructure E and (b) microstructure W. Circles represent theoretically calculated fractions, assuming that all variants are formed with equal statistical probability (randomly) during phase transformation. Because of symmetry, there are only 16 independent inter-variant interfaces and the "=" sign shows two equivalent inter-variant interfaces.

heterogeneous nucleation on inclusions or they might be extensions of plates nucleated on grain boundaries that are not visible within the section plane. However, the mechanism for the formation of finger-like austenite morphologies from the allotriomorphic films has been a matter of debate. Different mechanisms have been proposed to explain these protrusions, namely (i) preferential growth of austenite along the ferrite sub-boundaries [43], (ii), sympathetic nucleation [44] and (iii) the instability mechanism [45,46]. The first mechanism can, however, be ruled out here, as the ferrite is expected to be free of any internal sub-boundaries at 1370 °C. The observation of an austenite-austenite low-angle boundary with a misorientation of about 1° suggests the edge-to-edge sympathetic nucleation of austenite (Fig. 4a). On the other hand, absence of any austenite-austenite boundary in the protrusions, illustrated in Fig. 4b, is consistent with the instability mechanism. This suggests the co-operation of sympathetic nucleation and the instability mechanism.

4.2. Boundaries/interphases characteristics

The phase transformation path affects the characteristics of austenite-ferrite and austenite-austenite interfaces (Figs. 5–11). This can be attributed to distinct phase transformation mechanisms taking place in microstructures E and W.

4.2.1. Austenite-ferrite interfaces

The phase transformation path (i.e., cooling rate) remarkably influences the population of K-S and N-W austenite-ferrite interfaces. For example, microstructure W displays a significantly higher content of K-S/N-W interfaces (39%) compared with microstructure E (16%). This is mostly due to the change in the cooling rate, which changes the mechanism of nucleation and growth of austenite during the phase transformation. Austenite preferentially nucleates on the prior ferrite grain boundaries, potentially forming a specific interface configuration on either side

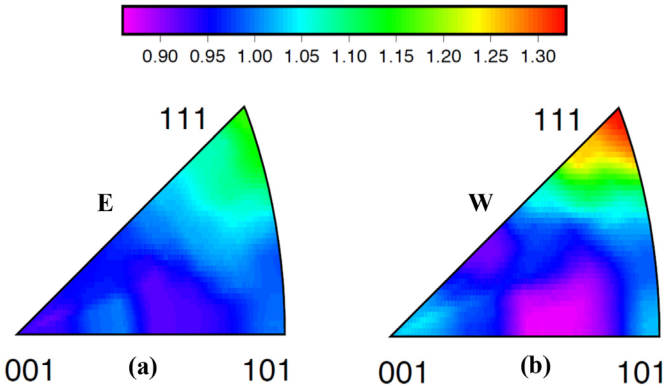

Fig. 13. 2-D distribution of the austenite-austenite grain boundary planes with different misorientation angles and axes excluding Σ3 and Σ9 boundaries for (a) for microstructure E and (b) for microstructure W. The colour scale values are in MRD. (For interpretation of the references to colour in this figure legend, the reader is referred to the Web version of this article.)

of the boundaries depending on cooling rate. The austenite nuclei interfaces can be classified into three configurations, having: (i) rational interfaces with both ferrite grains at either side of the boundary; (ii) rational interface with only one grain and (iii) irrational interfaces with both of the two ferrite grains. The high cooling rate mostly promotes the formation of austenite nuclei with rational interfaces (types i and ii), while the irrational interfaces are mostly formed in slow cooling conditions [32,47]. In microstructure E, the phase transformation takes place in a relatively high temperature range (i.e., during cooling from ~1370 °C at a rate of 0.002 °C/s). In such a high temperature regime, the difference in the energy barrier for the austenite nucleation with a rational or irrational interface is not as great as at low temperatures. Therefore, both interfaces can potentially be formed, and ultimately not all of the ferrite-austenite interfaces will fully fulfil the K-S/N-W orientation relationship requirements. This may promote the formation of austenite nuclei with other (non-KS/NW) interface characteristics on slow cooling (microstructure E). By contrast, the air-cooling condition provides a relatively high undercooling suitable for Widmanstätten austenite nucleation resulting in a large fraction of K-S/N-W interfaces. In addition, the high cooling rate promotes intragranular austenite formation, which mostly appears to have K-S/N-W interfaces with the parent ferrite.

The austenite growth is dictated by the phase transformation mechanism. During slow cooling, the interface movement is largely controlled by alloying elements diffusion/partitioning, which may be enhanced across non-KS/NW interfaces due to their higher energy. A high cooling rate promotes a shear transformation, which ultimately leads to the directional growth of austenite nuclei along the K-S/N-W interfaces. Consequently, the overall fraction of K-S/N-W interfaces in microstructure W becomes higher than in microstructure E due to the change in the mechanism of both nucleation and growth.

Among the interfaces examined here, K-S is a more dominant OR than N-W in both microstructures. This could be explained through the formation of annealing twins during the ferrite to austenite transformation. The twin relationship in fcc crystals can be described by 180°/<112>. Therefore, the twin rotation of any K-S oriented austenite variant, having a 90°/<112> OR with the matrix [48], would also result in an austenite variant with K-S OR with parent ferrite. The initial orientation relationship is not, however, fully preserved during the twinning of an N-W austenite variant, as the angle-axis associated with N-W OR (i.e., 90.12°/<−0.348, 0.841, 0.413>) is different from 90°/<112> [48]. It should be noted that the presence of local elemental segregation is inevitable during a phase transformation, which may locally make the interface deviate from the ideal orientation relationship. It has also been demonstrated that small deviations from the ideal rational OR may give a better compromise between the overall atom matching and energy minimization in the interface [49].

In the misorientation angle range of 40–50°, austenite habit planes reveal a peak at the (111) orientation for both the E and W microstructures (Fig. 9a). Ferrite habit planes, however, show complex behaviour displaying two peaks at the positions of (110) and (111) (Fig. 9b). For rational ORs (i.e., K-S and N-W), ferrite and austenite terminate on (110) and (111) planes, respectively (Fig. 6), irrespective of the transformation route. These are crystallographically preferred planes for interfacial parallelism in the rational interfaces formed during the phase transformation, and are of the highest coordination number. Moreover, these planes are close to the predictions made based on Near-Coincidence Site (NCS) geometrical matching of bcc-fcc lattices [50–52]. The high frequency of these planes is also consistent with the minimum plane energy calculations using the first nearest neighbour broken bond model, revealing a minimum at the $(111)_{fcc}$ and $(110)_{bcc}$ planes [53]. The population of these planes is larger for the larger transformation rate, supporting the observation that microstructure W has a higher fraction of rational interphases.

Microstructure W contains allotriomorphic and intragranular austenite, which form in different transformation regimes during air-cooling. The allotriomorphic austenite is formed at an early stage of transformation (i.e., at lower undercooling), while the intragranular austenite is transformed at a comparatively higher undercooling (i.e., in the lower temperature regime). The intragranular austenite has a relatively higher fraction of K-S/N-W interfaces (42%) compared with the allotriomorphic austenite (23%). The plane distribution peaks are also sharper for the intragranular austenite compared with the allotriomorphic austenite (see Figs. 7 and 8). The above observations suggest that most K-S/N-W interfaces present in microstructure W belong to the intragranular elongated austenite rather than allotriomorphic austenite. In other words, the austenite that transformed in the lower temperature regime (intragranular elongated austenite) has more K-S/N-W interphase area than the allotriomorphic austenite.

The current work shows that habit planes for the non-KS/NW interphases mostly terminate on (111) planes for both austenite and ferrite (Figs. 6–8). While this is an energetically and crystallographically preferred plane for austenite, it is not generally the case for ferrite. The predominance of (111) planes in ferrite might be related to its texture, as recently observed in a fully ferritic microstructure having a strong {111} fibre texture [8]. This can be, however, ruled out here, as the ferrite has a {001}<110> texture in both the E and W microstructures (see Figs. 2b and 3b). There are also some reports that (111) ferrite surfaces have the minimum energy at low temperatures, which was mostly attributed to the absorption of oxygen on these surfaces [54]. Nevertheless, it is clear that the abovementioned termination of ferrite on (111) planes in non-KS/NW interphases in duplex stainless steel is an area which requires further work.

4.2.2. Austenite-austenite CSL boundaries

Σ3 boundaries are the most populated austenite-austenite boundaries in the E and W microstructures. The fraction of these boundaries is higher in the equiaxed austenite morphology compared with the Widmanstätten austenite. Generally, the difference in the Σ3 population may be attributed to different factors such as crystallographic texture [55], grain size [56], composition [57], and heat treatment profile [58]. The crystallographic texture cannot play a role here as both austenite morphologies have similar overall texture (Figs. 2 and 3). Grain refinement can lead to an enhanced concentration of CSL boundaries [56]. However, the fine Widmanstätten austenite reveals fewer Σ3 boundaries than coarse equiaxed austenite grains. This could be partly due to their distinct morphology. The equiaxed austenite is transformed at a relatively high temperature during slow cooling, mostly representing a diffusional transformation. The formation of the Widmanstätten austenite takes place through a semi-shear transformation due to faster cooling rate. These distinct phase transformation profiles lead to a change in the austenite composition, as the extent of alloying element partitioning during the diffusional transformation is higher than in the semi-shear mode. EDS analysis reveals that the equiaxed austenite is enriched in Ni but has less Cr compared with the Widmanstätten morphology (Table 4). In general, elemental partitioning between austenite and ferrite is greater in microstructure E than microstructure W. However, the stacking fault energies of the equiaxed and Widmanstätten austenite at room temperature, calculated using a thermodynamic approach described in Ref. [59], are relatively close (28 and 31 mJ/m^2, respectively). Assuming that the change in SFE with temperature follows a similar trend for both the austenite compositions/morphologies, no significant difference in their SFEs would be expected at the temperature range where they are formed.

Σ3 boundaries are formed through reorientation of a grain to a twin orientation in fcc materials to reduce the overall grain boundary energy during grain growth and/or facilitate dislocation absorption during recrystallization [60]. The latter is not relevant here as the austenite transforms from ferrite with a low dislocation content in a relatively high temperature regime. It was demonstrated that the heat treatment profile significantly influences the population of CSL boundaries in a single phase Ni alloy. A slow heating and cooling profile remarkably enhances the CSL boundary populations suggesting that kinetic factors play a role in the twin formation [58]. In a similar way, the current results show that when the ferrite to austenite transformation takes place over a longer period (i.e., during slow cooling compared to air-cooling), a higher population of Σ3 boundaries forms in duplex stainless steels. In addition to the kinetic factor, it appears that the growth mode of the austenite plates also affects the Σ3 population. Close inspection of both the microstructures studied reveals that the annealing twins are mostly observed in the equiaxed austenite and allotriomorphic austenite in the microstructure W (see Figs. 2 and 3). Interestingly, the intragranular elongated austenite largely appears free of annealing twins. Thus, the Σ3 formation seems to play a role in the diffusional growth of austenite to facilitate the ferrite to austenite transformation. By contrast, Σ3 boundaries are rarely observed within the elongated intragranular austenite islands, which are expected to form through a semi-shear transformation.

Slow cooling also leads to a higher fraction of coherent Σ3 boundaries (Fig. 10). During slow cooling, the formation of equiaxed austenite takes place in the high temperature regime, where sufficient thermal energy is provided for Σ3 boundaries to shift towards the (111) twist orientation having the minimum energy configuration. Moreover, the presence of dislocations in the Widmanstätten austenite is expected due to the (semi-)shear transformation and the residual stresses associated with the fast cooling (see Fig. 4), which may cause Σ3 boundaries to lose their coherency. The abundance of Σ3s leads to a higher fraction of Σ9 boundaries within the equiaxed austenite compared with its Widmanstätten counterpart, as the latter boundaries are largely formed as a result of the intersection of two Σ3s, which do not share a common rotation axis. Σ9 grain boundary planes, therefore, lie in the zone of tilt boundaries due to geometrical constraints rather than boundary energy minimization [61] (Fig. 11). Furthermore, because of the anisotropic shapes of the intragranular austenite, and the condition in which the twin is formed within the grain, it is difficult to create a long twin. If the twins are randomly placed, it is very unlikely they would be on the long axis and very likely they would traverse the shorter dimension. This can be observed in Fig. 3a.

Table 4
The content of major alloying elements (wt. %) in different phases under different phase transformation paths measured using energy dispersive spectroscopy technique.

Microstructure	Phase	Ni	Cr	Mo	Mn
E (Furnace cooled)	austenite	6.4	20.4	2.2	2.0
	ferrite	3.7	25.0	3.7	1.8
W (Air cooled)	austenite	6.1	22.9	2.5	2.1
	ferrite	5.1	23.5	3.3	1.9

4.2.3. Austenite-austenite intervariant boundaries

The intervariant boundary plane distributions display more frequent {111} orientations than other plane orientations for both the E and W microstructures (Fig. 13). However, this trend is markedly stronger for the Widmanstätten austenite compared with the equiaxed austenite. In the theoretical K-S and N-W ORs, a $\{110\}_{bcc}$ plane coincides with a $\{111\}_{fcc}$ plane, which makes two growing austenite variants, most likely, intersect on the {111} planes. For an intervariant boundary of 60°/[111], the {111} orientation represents the minimum energy position in the distribution [19]. However, the presence of a {111} orientation does not always signify a low energy configuration. In the case of 60°/[110], (111) appears to have a relatively high energy [19,40]. This suggests that the crystallographic constraints associated with the phase transformation have a greater influence on the grain boundary plane than the energy. This is more prominent in microstructure W, where the interfaces are highly controlled by the crystallographic constraints due to the (semi-)shear mode of transformation.

5. Conclusions

In this study, the effect of the phase transformation route on the characteristics of the microstructure, texture and interfaces formed during the ferrite-to-austenite phase transformation was investigated. The main findings are:

1- The ferrite texture in both the air-cooled (microstructure W) and furnace-cooled (microstructure E) states showed similar characteristics to the as-received condition, being composed of a strong rotated cube {001}<110> component. The Widmanstätten and equiaxed austenite displayed a very similar texture to the as-received condition, comprising the Cube, Brass, Copper and Goss components. This was largely attributed to a "texture memory" effect.
2- Microstructure W displayed a significantly higher fraction of K-S/N-W interfaces (39%) compared with microstructure E (16%). This was mostly due to the cooling rate induced change in the mechanism of nucleation and growth of austenite during the phase transformation.
3- The K-S OR was more common than the N-W OR in both of the microstructures studied. This was attributed to the formation of annealing twins during the ferrite to austenite transformation.
4- For K-S/N-W ORs, ferrite and austenite terminated on (110) and (111) habit planes, respectively, irrespective of the transformation route. The population of these planes, however, was greater for the higher transformation rate,

consistent with conclusion 2, that microstructure W had a higher concentration of K-S/N-W interphases.

5- The allotriomorphic austenite present within microstructure W had a relatively lower fraction of K-S/N-W interphases (i.e., 23%) compared with the co-existing intragranular elongated austenite (i.e., 42%). This might be related to the differences in the nucleation and growth mechanism of these microstructure constituents, caused by their formation in different temperature regimes on cooling.
6- The most probable interphase planes associated with non-KS/NW ORs were (111) for both austenite and ferrite in microstructure E and W.
7- The fraction of Σ3 boundaries, as the most frequent austenite-austenite boundaries in both microstructures, was greater in microstructure E than in W. This was mainly attributed to the kinetics factor and the growth mode of the austenite plates during the phase transformation. The formation of Σ3s seemed to play an important role in the diffusional growth of equiaxed austenite to facilitate the ferrite to austenite transformation. Σ3 boundaries were, however, rarely observed within the elongated intragranular austenite islands present in microstructure W, which were expected to form through a semi-shear transformation.
8- Σ9 boundaries were of a tilt character because of geometrical constraints rather than boundary energy minimization.
9- The austenite intervariant boundary plane distributions displayed more frequent {111} orientations than other planes for both the E and W microstructures. This trend was much stronger for the Widmanstätten austenite compared with its equiaxed counterpart.

Acknowledgements

The present work was carried out with the support of the Deakin Advanced Characterisation Facility. Financial support provided by the Australian Research Council is gratefully acknowledged.

References

[1] T. Watanabe, Grain boundary engineering: historical perspective and future prospects, J. Mater. Sci. 46 (2011) 4095–4115.
[2] C.A. Schuh, M. Kumar, W.E. King, Analysis of grain boundary networks and their evolution during grain boundary engineering, Acta Mater. 51 (2003) 687–700.
[3] V. Randle, Twinning-related grain boundary engineering, Acta Mater. 52 (2004) 4067–4081.
[4] M. Michiuchi, H. Kokawa, Z.J. Wang, Y.S. Sato, K. Sakai, Twin-induced grain boundary engineering for 316 austenitic stainless steel, Acta Mater. 54 (2006) 5179–5184.
[5] D.A. Porter, K.E. Easterling, Phase Transformation in Materials, Chapman & Hall, Boundary Row, London, 1992, pp. 291–308.
[6] R.E. Reed-Hill, R. Abbaschian, Physical metallurgy principles, (1973).
[7] H.K.D.H. Bhadeshia, D.V. Edmonds, The bainite transformation in a silicon steel, Metal Trans A 10 (1979) 895–907.
[8] H. Beladi, G.S. Rohrer, The relative grain boundary area and energy distributions in a ferritic steel determined from three-dimensional electron backscatter diffraction maps, Acta Mater. 61 (2013) 1404–1412.
[9] H. Beladi, G.S. Rohrer, A.D. Rollett, V. Tari, P.D. Hodgson, The distribution of intervariant crystallographic planes in a lath martensite using five macroscopic parameters, Acta Mater. 63 (2014) 86–98.
[10] H. Beladi, G.S. Rohrer, The role of thermomechanical routes on the distribution of grain boundary and interface plane orientations in transformed microstructures, Metal. Mater. Trans. A 48 (2017) 2781–2790.
[11] I. Lischewski, G. Gottstein, Nucleation and variant selection during the α–γ–α phase transformation in microalloyed steel, Acta Mater. 59 (2011) 1530–1541.
[12] Z. Liu, Y. Kobayashi, J. Yang, K. Nagai, M. Kuwabara, "In-situ" observation of the delta/gamma phase transformation on the surface of low carbon steel containing phosphorus at various cooling rates, ISIJ Int. 46 (2006) 847–853.
[13] R.N. Gunn, Duplex Stainless Steels: Microstructure, Properties and Applications, Woodhead Publishing, Cambridge, 1997.
[14] B. Verhaeghe, F. Louchet, B. Doisneau-Cottignies, Y. Bréchet, J.P. Massoud, Micromechanisms of deformation of an austenoferritic duplex stainless steel, Phil. Mag. A 76 (1997) 1079–1091.
[15] N. Haghdadi, P. Cizek, H. Beladi, P.D. Hodgson, Dynamic restoration processes in a 23Cr-6Ni-3Mo duplex stainless steel: Effect of austenite morphology and interface characteristics, Metal. Mater. Trans. A 48 (2017) 4803–4820.
[16] K. Tsuzaki, H. Matsuyama, M. Nagao, T. Maki, High-strain rate superplasticity and role of dynamic recrystallization in a superplastic duplex stainless steel, Mater. Trans., JIM 31 (1990) 983–994.
[17] N. Haghdadi, D. Abou-Ras, P. Cizek, P.D. Hodgson, A.D. Rollett, H. Beladi, Austenite-ferrite interface crystallography dependence of sigma phase precipitation using the five-parameter characterization approach, Mater. Lett. 196 (2017) 264–268.
[18] G.S. Rohrer, D.M. Saylor, B. El Dasher, B.L. Adams, A.D. Rollett, P. Wynblatt, The distribution of internal interfaces in polycrystals, Z Metallkd 95 (2004) 197–214.
[19] H. Beladi, N.T. Nuhfer, G.S. Rohrer, The five-parameter grain boundary character and energy distributions of a fully austenitic high-manganese steel using three dimensional data, Acta Mater. 70 (2014) 281–289.
[20] H. Beladi, Q. Chao, G.S. Rohrer, Variant selection and intervariant crystallographic planes distribution in martensite in a Ti-6Al-4V alloy, Acta Mater. 80 (2014) 478–489.
[21] D.M. Saylor, B.S. El Dasher, A.D. Rollett, G.S. Rohrer, Distribution of grain boundaries in aluminum as a function of five macroscopic parameters, Acta Mater. 52 (2004) 3649–3655.
[22] B. Hutchinson, J. Komenda, G.S. Rohrer, H. Beladi, Heat affected zone microstructures and their influence on toughness in two microalloyed HSLA steels, Acta Mater. 97 (2015) 380–391.
[23] X. Fang, W. Yin, C. Qin, W. Wang, K.H. Lo, C.H. Shek, The interface character distribution of cold-rolled and annealed duplex stainless steel, Mater. Charac. 118 (2016) 397–404.
[24] H. Beladi, V. Tari, I.B. Timokhina, P. Cizek, G.S. Rohrer, A.D. Rollett, P.D. Hodgson, On the crystallographic characteristics of nanobainitic steel, Acta Mater. 127 (2017) 426–437.
[25] S.B. Lee, J.E. LeDonne, S.C.V. Lim, I.J. Beyerlein, A.D. Rollett, The heterophase interface character distribution of physical vapor-deposited and accumulative roll-bonded Cu–Nb multilayer composites, Acta Mater. 60 (2012) 1747–1761.
[26] N. Haghdadi, P. Cizek, H. Beladi, P.D. Hodgson, A novel high-strain-rate ferrite dynamic softening mechanism facilitated by the interphase in the austenite/ferrite microstructure, Acta Mater. 126 (2017) 44–57.
[27] S.I. Wright, R.J. Larsen, Extracting twins from orientation imaging microscopy scan data, J. Micros. 205 (2002) 245–252.
[28] D. Raabe, M. Ylitalo, Experimental investigation of the transformation texture in hot rolled ferritic stainless steel using single orientation determination, Metal. Mater. Trans. 27 (1996) 49–57.
[29] J.Y. Kang, B. Bacroix, H. Réglé, K.H. Oh, H.C. Lee, Effect of deformation mode and grain orientation on misorientation development in a body-centered cubic steel, Acta Mater. 55 (2007) 4935–4946.
[30] M.V. Kral, G. Spanos, Three-dimensional analysis of proeutectoid cementite precipitates, Acta Mater. 47 (1999) 711–724.
[31] R. Badji, B. Bacroix, M. Bouabdallah, Texture, Microstructure and anisotropic properties in annealed 2205 duplex stainless steel welds, Mater. Charac. 62 (2011) 833–843.
[32] W.B. Hutchinson, L. Ryde, P.S. Bate, Transformation textures in steels, Mater. Sci. Forum 495 (2005) 1141–1150.
[33] G. Kurdjumov, G. Sachs, Over the mechanisms of steel hardening, Z. Phys. 64 (1930) 325–343.
[34] Z. Nishiyama, Sci Rep Res Inst, vol. 23, Tohoku University, 1934–35, p. 638.
[35] A.B. Greninger, A.R. Troiano, The mechanism of martensite formation, JSME Trans. 185 (1949) 590–598.
[36] W. Pitsch, Der orientierungszusammenhang zwischen zementit und austenite, Acta Metall. 10 (1962) 897–900.
[37] E.C. Bain, The nature of martensite, Trans. AIME 70 (1924) 25–47.
[38] D.G. Brandon, The structure of high-angle grain boundaries, Acta Metall. 14 (1966) 1479–1484.
[39] J. Li, S.J. Dillon, G.S. Rohrer, Relative grain boundary area and energy distributions in nickel, Acta Mater. 57 (2009) 4304–4311.
[40] V. Randle, G.S. Rohrer, H.M. Miller, M. Coleman, G.T. Owen, Five-parameter grain boundary distribution of commercially grain boundary engineered nickel and copper, Acta Mater. 56 (2008) 2363–2373.
[41] K. Ameyama, G.C. Weatherly, K.T. Aust, A study of grain boundary nucleated widmanstätten precipitates in a two-phase stainless steel, Acta Metall. Mater. 40 (1992) 1835–1846.
[42] Y. Ohmori, K. Nakai, H. Ohtsubo, Y. Isshiki, Mechanism of widmanstätten austenite formation in a δ/γ duplex phase stainless steel, ISIJ Int. 35 (1995) 969–975.
[43] D. Phelan, R. Dippenaar, Instability of the delta-ferrite/austenite interface in low carbon steels: the influence of delta-ferrite recovery sub-structures, ISIJ Int. 44 (2004) 414–421.
[44] C.Y. Chen, H.W. Yen, J.R. Yang, Sympathetic nucleation of austenite in a Fe–22Cr–5Ni duplex stainless steel, Scripta Mater. 56 (2007) 673–676.
[45] W.W. Mullins, R.F. Sekerka, Morphological stability of a particle growing by diffusion or heat flow, J. Appl. Phys. 34 (1963) 323–329.
[46] R.D. Townsend, J.S. Kirkaldy, Widmanstatten ferrite formation in Fe-C alloys, Trans. ASM 61 (1968) 605–619.

[47] Y. Adachi, K. Hakata, K. Tsuzaki, Crystallographic analysis of grain boundary Bcc-precipitates in a Ni–Cr alloy by FESEM/EBSD and TEM/Kikuchi line methods, Mater. Sci. Eng. 412 (2005) 252–263.
[48] J.J. Jonas, Y. He, G. Langelaan, The rotation axes and angles involved in the formation of self-accommodating plates of Widmanstätten ferrite, Acta Mater. 72 (2014) 13–21.
[49] C.H. Shek, J.K. Lai, K.W. Wong, C. Dong, Early-stage widmanstatten growth of the γ phase in a duplex steel, Metall. Mater. Trans. 31 (2000) 15–19.
[50] G. Miyamoto, R. Hori, B. Poorganji, T. Furuhara, Crystallographic analysis of proeutectoid ferrite/austenite interface and interphase precipitation of vanadium carbide in medium-carbon steel, Metall. Mater. Trans. 44 (2013) 3436–3443.
[51] T. Furuhara, T. Maki, K. Oishi, Interphase boundary structure with irrational orientation relationship formed in grain boundary precipitation, Metall. Mater. Trans. 33 (2002) 2327–2335.
[52] Q. Liang, W.T. Reynolds, Determining interphase boundary orientations from near-coincidence sites, Metall. Mater. Trans. 29 (1998) 2059–2072.
[53] J.K. Mackenzie, A.J.W. Moore, J.F. Nicholas, Bonds broken at atomically flat crystal surfaces-I: face-centred and body-centred cubic crystals, J. Phys. Chem. Solid. 23 (1962) 185–196.
[54] B. Mills, M. McLean, E.D. Hondros, Surface-energy anisotropy of 3 percent Si-Fe, Philos. Mag. 27 (1973) 361–368.
[55] G. Gottstein, F. Schwarzer, On the orientation dependence of grain boundary energy and mobility, Mater. Sci. Forum 94 (1992) 187–208.
[56] T. Watanabe, H. Fujii, H. Oikawa, K.I. Arai, Grain boundaries in rapidly solidified and annealed Fe-6.5 mass% Si polycrystalline ribbons with high ductility, Acta Metal.f 37 (1989) 941–952.
[57] V. Randle, The Role of the Coincidence Site Lattice in Grain Boundary Engineering, Inst. Materials, London, 1996.
[58] V. Randle, Influence of kinetic factors on distribution of grain boundary planes in nickel, Mater. Sci. Technol. 7 (1991) 985–990.
[59] R.E. Schramm, R.P. Reed, Stacking fault energies of seven commercial austenitic stainless steels, Metall. Mater. Trans. 6 (1975) 1345–1351.
[60] W. Form, G. Gindraux, New concepts of annealing-twin formation in face centred cubic metals, J. Inst. Met. 101 (1973) 85–93.
[61] G.S. Rohrer, V. Randle, C.S. Kim, Y. Hu, Changes in the five-parameter grain boundary character distribution in α-brass brought about by iterative thermomechanical processing, Acta Mater. 54 (2006) 4489–4502.